Journal of Computational Physics **170,** 830–848 (2001)
doi:10.1006/jcph.2001.6765, available online at http://www.idealibrary.com on IDEAL®

FDFD: A 3D Finite-Difference Frequency-Domain Code for Electromagnetic Induction Tomography[1]

Nathan J. Champagne II, James G. Berryman, and H. Michael Buettner

Lawrence Livermore National Laboratory, Livermore, California 94551-9900

Received June 20, 2000; revised March 1, 2001

A new 3D code for electromagnetic induction tomography with intended applications to environmental imaging problems has been developed. The approach consists of calculating the fields within a volume using an implicit finite-difference frequency-domain formulation. The volume is terminated by an anisotropic perfectly matched layer region that simulates an infinite domain by absorbing outgoing waves. Extensive validation of this code has been done using analytical and semianalytical results from other codes, and some of those results are presented in this paper. The new code is written in Fortran 90 and is designed to be easily parallelized. Finally, an adjoint field method of data inversion, developed in parallel for solving the fully nonlinear inverse problem for electrical conductivity imaging (e.g., for mapping underground conducting plumes), uses this code to provide solvers for both forward and adjoint fields. Results obtained from this inversion method for high-contrast media are encouraging and provide a significant improvement over those obtained from linearized inversion methods.

1. INTRODUCTION

Although electromagnetic surveying techniques of both the electrical-current-injection type and the magnetic-field type have been well known for many years [1], the results were typically only semiquantitative, and efforts to turn these surveys into true quantitative 3D maps of electrical conductivity distribution in the subsurface have only been

[1] This work was performed under the auspices of the U.S. Department of Energy by the University of California, Lawrence Livermore National Laboratory under Contract W-7405-ENG-48 and supported specifically by the Environmental Management Science Program of the Office of Environmental Management and the Office of Energy Research, and with additional support from the Office of Basic Energy Sciences.

0021-9991/01 $35.00

attempted in the past 10 to 15 years [2–4]. One of the main reasons for this delay has surely been the necessity of using large computer memories and fast computing machines, because it does not take a very large 3D forward modeling problem in typical geophysical settings to swamp even today's most advanced computing platforms. Of course, 3D electromagnetic codes for various other applications are commonly available. One well-developed example of such a multipurpose 3D electromagnetic code that has been tested and used by many researchers is the 3D-MAFIA group of codes [5, 6]. These codes were developed principally for laboratory-scale design studies and other forward modeling purposes, but have limitations (such as the need for carefully designed nonreflecting boundary conditions [7]) for use in geophysical imaging and data-inversion applications. However, recent work on 3D magnetotellurics and controlled source electromagnetic underground imaging as it has been pursued within the geophysics community includes papers by Hohmann [8], Mackie *et al.* [9], Torres-Verdin and Habashy [10], Newman and Alumbaugh [11–13], and Smith [14, 15]. A recent review of the state of the art in 3D EM modeling for such geophysical applications including detailed comparisons of results [16] demonstrated both the limitations and the lack of consensus concerning the best methods for computing EM fields in applications to very inhomogeneous, strongly conducting earth materials.

Our specific interest here is in controlled source electromagnetic induction tomography (EMIT), which is a comparatively new geophysical imaging method that has been pursued with extensive field studies in recent years [3, 4, 17, 18]. But our ability to turn these field data into well-resolved images of conducting inclusions, structures, and fluid plumes in the earth has been hampered by the requirements for high accuracy forward computations at useful levels of resolution. (We expand on the unique physical characteristics and imaging abilities of EMIT in Section 2.) For these applications, we have developed a new 3D code for use in electromagnetic induction tomography, especially for environmental imaging problems. The finite-difference frequency-domain (FDFD) formulation is based on that in [19], and an anisotropic perfectly matched layer (PML) approach [7, 20] is used to specify the nonreflecting boundary conditions. The unique features of the method include perfectly matched layer boundaries [7, 20], specifically tailored to provide optimum results in the target frequency range (the lower kHz regime), and code structure that permits convenient computation of the adjoint field operator (which is needed for the data-inversion method developed in parallel [21]).

Section 2 introduces the electromagnetic induction tomography problem in more detail. Section 3 describes the algorithm implemented in the code. Section 4 gives a series of examples to provide code validation in various relevant limiting cases. Section 5 discusses how the code has been used in the adjoint field approach to the data-inversion problem for electromagnetic induction tomography and is followed by our conclusions.

2. ELECTROMAGNETIC INDUCTION TOMOGRAPHY

For enhanced recovery of oil and gas in the earth or for various types of environmental cleanup efforts, it is often desirable to obtain images of conducting fluids underground. The porous earth and some typical pore fluids like hydrocarbons tend to be comparatively poor conductors, but other pore fluids that may be used in the extraction process (such as brines) may be quite good electrical conductors. So imaging of conducting plumes

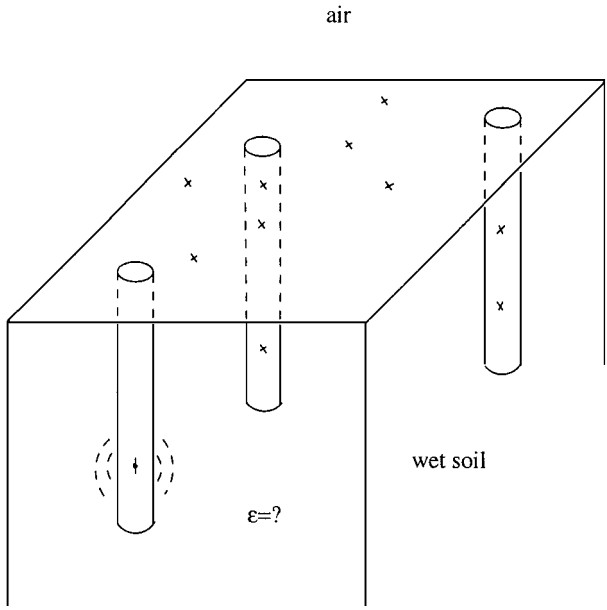

FIG. 1. A possible EMIT experimental setup. Three boreholes surround the volume where we wish to image the electrical conductivity. A z-directed dipole transmitter is deployed in one borehole, indicated in the lower left. The data are then gathered either in the other boreholes or at the surface or both, indicated by x's. A survey is performed by repeating this process using a number of different transmitter locations. The imaginary part of $\varepsilon(x)$ is proportional to the electrical conductivity distribution in the medium and is what we want to reconstruct from the measured magnetic field data.

(in real time if possible) is often a goal for monitoring of reservoirs and site characterization. Figure 1 illustrates what might be a typical configuration if three boreholes are available for the magnetic field data collection. The source is a magnetic field generated with current in wire coils. Received signals are the measured (small) changes in magnetic field in other boreholes, or at the surface of the earth.

Another EM field method that might also be used in similar circumstances is ground penetrating radar (GPR) [22, 23]. However, this method employs EM fields at frequencies in the range of 100 MHz or higher, whereas EMIT uses frequencies usually in the range of 1–10 kHz. At 100 MHz and above, it is a good approximation to think of GPR as a wave-propagation method, although the wave does not penetrate very far into the earth when the earth is wet and the wetting agent is a conductor because it is then highly attenuated. At 1–10 kHz, it is a good approximation to think of EMIT as a diffusion process—definitely not a wave-propagation process. Then the imaginary part of the complex dielectric constant ε is significantly larger than the real part, and so wave propagation gives way to diffusion. Because the frequencies are so much lower, the diffusing magnetic fields penetrate farther into the earth than a GPR signal can propagate, while behaving rather differently from EM signals at either higher frequencies (GHz) or much lower (quasistatic) frequencies (dc). These differences are what make the EMIT method useful, but also require some special efforts to construct EM codes that behave as they should in the proper frequency regime.

Dorn *et al.* [21] have shown how to invert EMIT data using an adjoint field method, and the inversion scheme makes direct use of the code that we now describe. The results obtained from this inversion method for high-contrast media are encouraging and pro-

vide a significant improvement over results obtained from linearized inversion methods [3].

3. FDFD ALGORITHM

The goal of this code development effort is to produce an accurate and efficient forward simulation for EM fields that can then be easily used for inversion of EMIT field data. The FDFD formulation presented here is an extension to lossy media of a method developed for lossless media in [19]. The mesh-truncation approach involves using an anisotropic absorbing PML following the ideas in [7, 24]. The absorbing regions have material parameters similar to those proposed in [25]. The code is written in Fortran 90, and ease of portability to various high performance computing platforms has been one of our design criteria throughout its development.

3.1. *Finite-Difference, Frequency-Domain Formulation*

To develop a system of equations to determine the electric and magnetic fields within a volume, the integral form of Maxwell's curl equations (Ampère's and Faraday's laws),

$$\oint_C \mathbf{H} \cdot d\ell = j\omega \int_S (\bar{\varepsilon} \cdot \mathbf{E}) \cdot \hat{\mathbf{n}} dS + \int_S \mathbf{J} \cdot \hat{\mathbf{n}}\, dS \tag{1}$$

and

$$\oint_C \mathbf{E} \cdot d\ell = -j\omega \int_S (\bar{\mu} \cdot \mathbf{H}) \cdot \hat{\mathbf{n}}\, dS - \int_S \mathrm{M} \cdot \hat{\mathbf{n}}\, dS, \tag{2}$$

are used. Here $\mathbf{J}$ is the impressed electric-current density, $\mathbf{M}$ is the impressed magnetic-current density, $\bar{\varepsilon}$ and $\bar{\mu}$ are diagonal dyads of dielectric permittivity and magnetic permeability, respectively, and C is the boundary of the open surface S. The integrals in (1) and (2) are applied to discrete elements (rectangular blocks) within the volume assuming approximately constant fields within each block and using the elementary relations

$$\int_{-a/2}^{a/2} \mathbf{f} \cdot d\ell \to a f_m \tag{3}$$

and

$$\int_{-a/2}^{a/2} \int_{-b/2}^{b/2} \mathbf{f} \cdot \hat{\mathbf{n}}\, dS \to ab f_m, \tag{4}$$

where f_m is a center value associated with the mth cell shown in Fig. 2. Note that the discrete electric field is located at the center of an edge, and the discrete magnetic field flows through the centroid of a face. Also, the mth cell is normally referred to as cell (i, j, k), but for notational convenience, a cell mapping using symbols such as u, d, l, r, f, b (for up, down, left, right, front, back, respectively) to specify the six cells surrounding the mth cell is used. This mapping is presented in Table I. Cells other than the six cells adjacent to the six faces may also be labeled using the same mapping. For example, relative to cell m, cell df is cell $(i-1, j, k-1)$ and cell dlb is cell $(i-1, j-1, k+1)$.

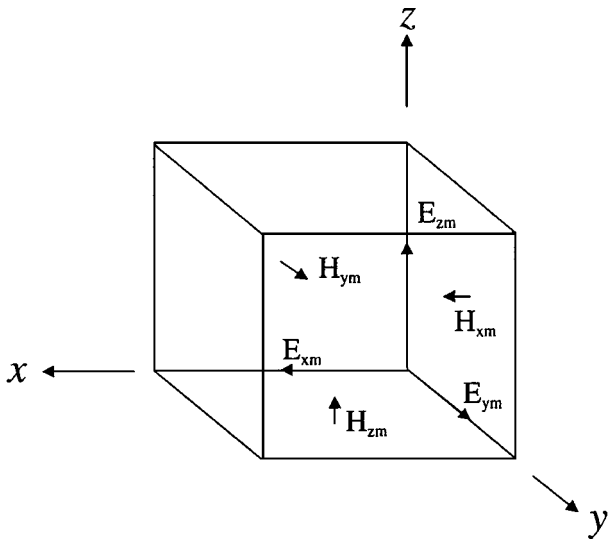

FIG. 2. The field quantities associated with the mth cell $(i,\ j,\ k)$.

The discretized forms of (1) and (2) result in an equation for each field component. The resulting equations are cumbersome; however, presenting each expression using matrices provides a compact form. Thus, extending the lossless and isotropic methods of Beilenhoff *et al.* [19] to our case of lossy and anisotropic media, and using notation defined in the Appendix, (1) and (2) become

$$\boldsymbol{A}^T \boldsymbol{D}_{\bar{\ell}} \vec{h} = j\omega\varepsilon_0 \boldsymbol{D}_{A\varepsilon}\, \vec{e} + \boldsymbol{D}_{\bar{A}}\, \vec{j} \tag{5}$$

and

$$\boldsymbol{A} D_\ell\, \vec{e} = -j\omega\mu_0 \boldsymbol{D}_A\, D_\mu\, \vec{h} - \boldsymbol{D}_A\, \vec{m}, \tag{6}$$

respectively. The apparent lack of symmetry in the pair of equations (5) and (6) arises from differences in the method of discretizing ε and μ on the staggered grid (see the Appendix for details). Solving for the magnetic field (to eliminate it from the equations) in (6) and then substituting the result in (5) yield

$$\boldsymbol{A}^T \boldsymbol{D}_{\bar{\ell}} \boldsymbol{D}_\mu^{-1} \boldsymbol{D}_A^{-1} \boldsymbol{A} D_\ell \vec{e} - k_0^2\, \boldsymbol{D}_{A\varepsilon}\, \vec{e} = -j\omega\mu_0\, \boldsymbol{D}_{\bar{A}} \vec{j} - \boldsymbol{A}^T \boldsymbol{D}_{\bar{\ell}} \boldsymbol{D}_\mu^{-1} \vec{m}, \tag{7}$$

TABLE I
Labels for Cells Surrounding
***m* = Cell (*i, j, k*)**

$d =$ cell $(i-1,\ j, k)$	$u =$ cell $(i+1,\ j, k)$
$l =$ cell $(i,\ j-1, k)$	$r =$ cell $(i,\ j+1, k)$
$f =$ cell $(i,\ j, k-1)$	$b =$ cell $(i,\ j, k+1)$

which has a form entirely analogous to that commonly used in finite-element codes, i.e.,

$$\boldsymbol{\nabla} \times \left(\bar{\mu}_r^{-1} \cdot \boldsymbol{\nabla} \times \mathbf{E}\right) - k_0^2 \bar{\varepsilon}_r \cdot \mathbf{E} = -j\omega\mu_0 \mathbf{J} - \boldsymbol{\nabla} \times \bar{\mu}_r^{-1} \cdot \mathbf{M}, \tag{8}$$

even though our goal here is to develop a finite-difference code.

A problem commonly observed in numerical computations of Maxwell's equations arises because of a possible resonance at zero frequency. If this occurs, the resulting matrix has an eigenvalue at zero and therefore is neither positive definite nor invertible. For the geometries considered here, the fields for resonant frequency of 0 Hz are generated only by electric charge within the volume. Such charges may develop as an artifact of numerical roundoff when evaluating the vector wave equation—especially at lower frequencies (see, for example, Smith [14]). This problem is avoided here by eliminating any charge within the volume using a term analogous to

$$\boldsymbol{\nabla}[\boldsymbol{\nabla} \cdot (\bar{\varepsilon}_r \cdot \mathbf{E})] = \mathbf{0}, \tag{9}$$

forcing the gradient of the charge density $\rho = \boldsymbol{\nabla} \cdot (\bar{\varepsilon}_r \cdot \mathbf{E})$ to be zero. The numerical implementation is achieved by starting from Gauss's law for the electric field in integral form,

$$\int_V \boldsymbol{\nabla} \cdot (\bar{\varepsilon}_r \cdot \mathbf{E})\, dV = \oint_S (\bar{\varepsilon}_r \cdot \mathbf{E}) \cdot \hat{\mathbf{n}}\, dS = 0, \tag{10}$$

to arrive at the discretized matrix expression

$$\left[\boldsymbol{D}_\ell^{-1} \boldsymbol{D}_{A\varepsilon}^* \boldsymbol{B}^T \left(\boldsymbol{D}_{V\varepsilon\varepsilon}^{-1} \boldsymbol{B} \boldsymbol{D}_{A\varepsilon}\right)\right] \vec{e} = \vec{0}, \tag{11}$$

where the matrices in parentheses arise from discretizing (10), while the remaining matrices in the square brackets arise from discretizing (9) after the application of an integral identity. The matrix $\boldsymbol{B}$ (not to be confused with the magnetic-flux density, or magnetic induction, $\mathbf{B}$) is also defined in the Appendix. When (11) is added to (7), the result is

$$\begin{aligned} &\left(\boldsymbol{A}^T \boldsymbol{D}_{\bar{\ell}} \boldsymbol{D}_\mu^{-1} \boldsymbol{D}_A^{-1} \boldsymbol{A} \boldsymbol{D}_\ell + \boldsymbol{D}_\ell^{-1} \boldsymbol{D}_{A\varepsilon}^* \boldsymbol{B}^T \boldsymbol{D}_{V\varepsilon\varepsilon}^{-1} \boldsymbol{B} \boldsymbol{D}_{A\varepsilon} - k_0^2 \boldsymbol{D}_{A\varepsilon}\right) \vec{e} \\ &\quad = -j\omega\mu_0 \boldsymbol{D}_{\bar{A}} \vec{j} - \boldsymbol{A}^T \boldsymbol{D}_{\bar{\ell}} \boldsymbol{D}_\mu^{-1} \vec{m}. \end{aligned} \tag{12}$$

However, a more symmetric form is obtained by multiplying throughout by $\boldsymbol{D}_\ell^{1/2}$ and then rewriting (12) as

$$\begin{aligned} &\left(\boldsymbol{D}_\ell^{1/2} \boldsymbol{A}^T \boldsymbol{D}_{\bar{\ell}} \boldsymbol{D}_\mu^{-1} \boldsymbol{D}_A^{-1} \boldsymbol{A} \boldsymbol{D}_\ell^{1/2} + \boldsymbol{D}_\ell^{-1/2} \boldsymbol{D}_{A\varepsilon}^* \boldsymbol{B}^T \boldsymbol{D}_{V\varepsilon\varepsilon}^{-1} \boldsymbol{B} \boldsymbol{D}_{A\varepsilon} \boldsymbol{D}_\ell^{-1/2} - k_0^2 \boldsymbol{D}_{A\varepsilon}\right) \boldsymbol{D}_\ell^{1/2} \vec{e} \\ &\quad = -j\omega\mu_0 \boldsymbol{D}_\ell^{1/2} \boldsymbol{D}_{\bar{A}} \vec{j} - \boldsymbol{D}_\ell^{1/2} \boldsymbol{A}^T \boldsymbol{D}_{\bar{\ell}} \boldsymbol{D}_\mu^{-1} \vec{m}. \end{aligned} \tag{13}$$

Note the appearance in these two equations of the complex conjugate matrix $\boldsymbol{D}_{A\varepsilon}^*$, which becomes necessary when losses are incorporated into ε.

3.2. *PML Formulation for Mesh Truncation*

The mesh is truncated using PMLs that absorb electromagnetic waves following the general ideas in [7]. The PML is a representation of anisotropic media satisfying

$$\mathbf{D} = \bar{\varepsilon}_{\mathrm{PML}} \cdot \mathbf{E} \quad \text{and} \quad \mathbf{B} = \bar{\mu}_{\mathrm{PML}} \cdot \mathbf{H}, \tag{14}$$

where

$$\bar{\varepsilon}_{\mathrm{PML}} = \bar{\varepsilon} \cdot \bar{\mathbf{\Lambda}} \quad \text{and} \quad \bar{\mu}_{\mathrm{PML}} = \bar{\mu} \cdot \bar{\mathbf{\Lambda}}. \tag{15}$$

The symbol $\bar{\mathbf{\Lambda}}$ stands for a diagonal dyad that has entries selected to absorb incident electromagnetic waves. The form of this dyadic quantity is determined by the normal to the PML interface. As an example, for a PML interface with a normal in the z direction, the form of $\bar{\mathbf{\Lambda}}$ is given by [20, 25],

$$\bar{\mathbf{\Lambda}}_z = \begin{bmatrix} a & 0 & 0 \\ 0 & a & 0 \\ 0 & 0 & 1/a \end{bmatrix}, \tag{16}$$

in which a is given by

$$a = 1 + \frac{f(x, y, z)}{1 + j\alpha\omega}, \tag{17}$$

where α is a constant and $f(x, y, z)$ is a function of position that is zero at the interface between the modeling space and the desired PML boundary. We have found through empirical studies that a suitable form for a is

$$a = 1 + \frac{f(x, y, z)}{1 + j\varepsilon_0\omega}, \tag{18}$$

where $f(x, y, z)$ is given by

$$f(x, y, z) = \frac{(1 - j)\beta}{\rho(x, y, z)}. \tag{19}$$

Here, $\rho(x, y, z)$ is the discretized distance from the modeling space/PML interface to the centroid of the cell of interest inside the PML. The parameter β is chosen to fix the amplitude of $f(x, y, z)$. To date, the best form of $\rho(x, y, z)$ has been found to be linear in the distance as determined by numerical experimentation so that $f(x, y, z)$ has an inverse type distribution, such as that in [27, 28].

3.3. *Solvers, Preconditioners, and Convergence Issues*

The resulting matrix equation is solved using the biconjugate gradient stabilized (BiCGSTAB) algorithm [29, 30] with simple diagonal preconditioning. The iterative solution converges very rapidly for lossless materials (see Beilenhoff *et al.* [19]). However, convergence results vary for lossy materials. When only electric losses are present (which is our main interest in this paper), there is little change in the rate of convergence. However, in the presence of magnetic losses, the matrix symmetry is lost, which significantly increases

the solution time—especially when it is necessary to use PML boundary conditions. Although this problem does not concern us here because of the target application, it could become important for other applications of the code. The problem may be alleviated to some extent by a new choice of preconditioner (see, for example, van der Vorst [30], Druskin *et al.* [31], and Newman and Alumbaugh [13]. In general, there is a continuing need for better solvers and preconditioners for lossy EM problems.

4. EXAMPLES

To demonstrate the accuracy and convergence properties of the code FDFD, we have tested various cases against analytical and semianalytical results. The set of results includes 1D, 2D, and 3D example problems.

A rectangular cavity (80 m $\times$ 5 m $\times$ 400 m) is shown in Fig. 3. There are 16 cells in the x direction, 1 cell in the y direction, and 80 cells in the z direction. The frequency of operation is 2 MHz, and the air/PML interfaces are located at $Z_1 = -100$ m and $Z_2 = -300$ m. The dominant (TE_{101}) mode of the cavity is launched (in the frequency domain) by imposing a sheet of E_y having unit magnitude at $Z_0 = -200$ m (which is sufficient to pick out the desired mode). The magnitude and phase of E_y, sampled at $x = 40$ m, are shown in Figs. 4 and 5. The FDFD results agree well with analytical calculations, the only significant deviations lying within the PML regions.

Next, a line of constant current (along the z axis) is placed at the center of a "square cavity" having square cross section in the xy plane and height b in the z direction as shown in Fig. 6. Each side has a length of 400 m (80 cells), and the height of the cavity is 5 m (1 cell). The frequency of operation is 2 MHz. The magnitude and phase of E_z are shown in Figs. 7 and 8. The data are plotted as a function of $\rho = x$ (for $y = 0$), which is positive when to the right of the line source or negative when to the left. The calculated and analytical data agree well, with the only significant deviations occurring in the PML region.

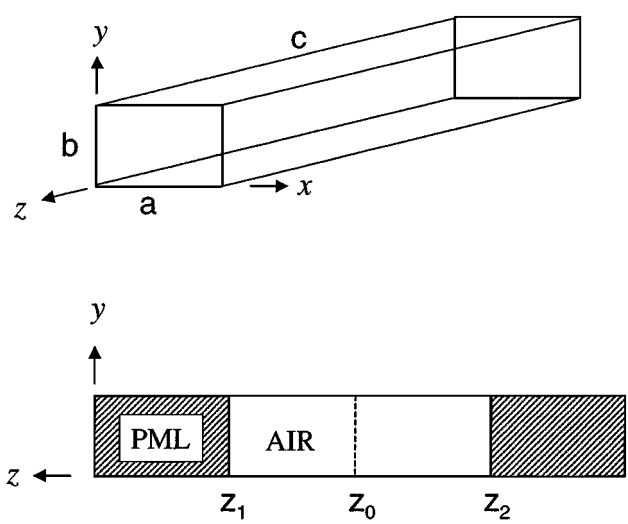

FIG. 3. A rectangular cavity with dimensions $a = 80$ m, $b = 5$ m, and $c = 400$ m. Also, $Z_0 = -200$ m, $Z_1 = -100$ m, and $Z_2 = -300$ m. The frequency of operation is 2 MHz.

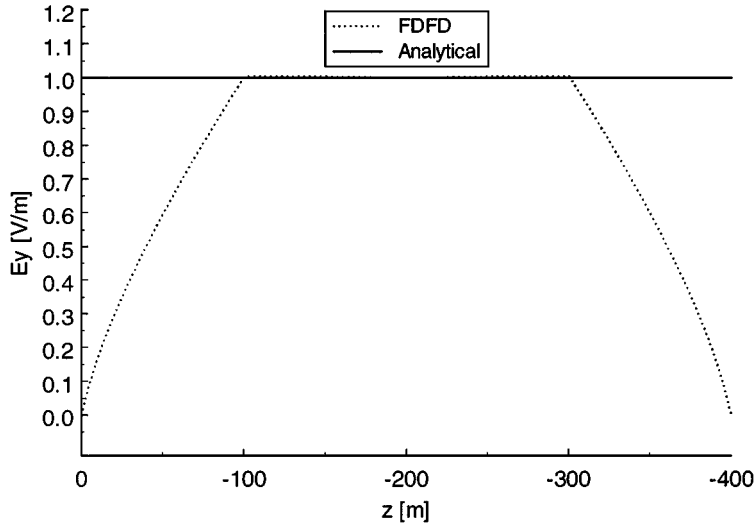

FIG. 4. The magnitude of E_y at $x = 40$ m for the rectangular cavity.

The following two sets of 2.5D examples (i.e., one-dimensional layered model but 3D fields computed using the full 3D code) shown here are based on the field geometry of Fig. 9. Receivers are inside a borehole in a layered medium with air above the free surface. The first example of a buried resistive layer has a 60-m-thick layer with conductivity = 0.3 S/m, a 25-m-thick layer with conductivity = 0.016 S/m, and an 85-m layer with conductivity = 0.3 S/m at the bottom of the model. Appropriately designed PML absorbing layers surround the modeled region on all six sides of the domain. The relative permittivity of all three earth layers is constant and assumed to be equal to 10.0. The frequency of the excitation is 1 kHz with the magnetic dipole transmitter located at the free surface with an offset of 5 m from the borehole. The finite-difference representation was chosen such that the unit spacing in

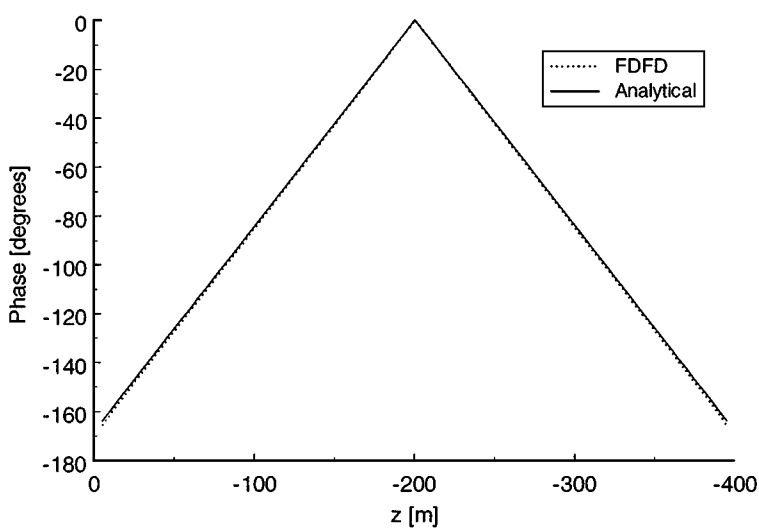

FIG. 5. The phase of E_y at $x = 40$ m for the rectangular cavity.

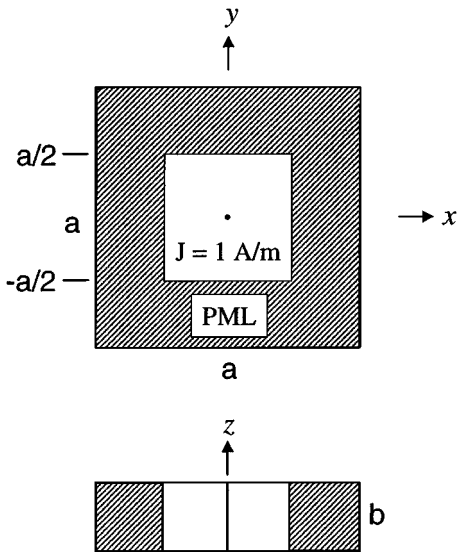

FIG. 6. A square cavity with xy dimensions: $a = 400$ m and height $b = 5$ m. The line of current is along the z axis. The frequency of operation is 2 MHz.

the earth model was 2.5 m, with 50 cells $\times$ 50 cells in the xy direction, and 10 layers of PML on those four sides. In the vertical direction, there were 68 cells in the earth model, 12 cells in the air above the free surface, and 10 more cells above and below for the PML layers. All PML cells are 10 m thick in the directions away from the earth model. The overall problem is then approximately $70 \times 70 \times 100 \simeq 500{,}000$ cells. The computations were performed on a DEC digital ultimate workstation (533 MHz), and required approximately 45 min of CPU time using about 260 iterations to achieve the convergence for the largest

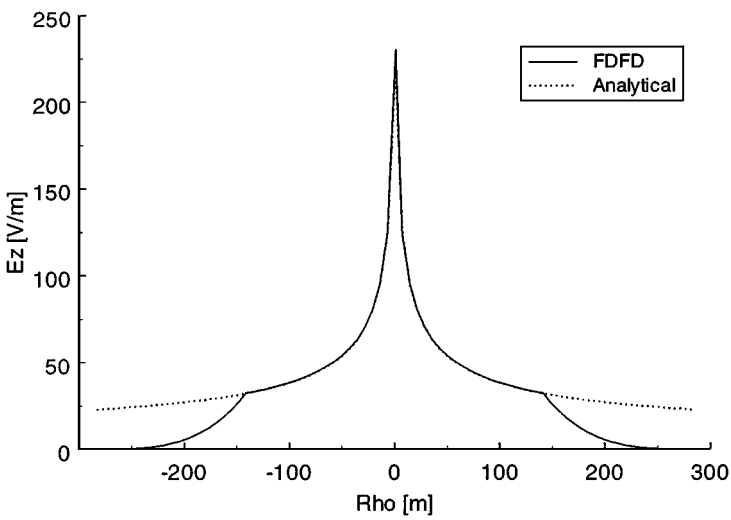

FIG. 7. The magnitude of E_z for the square cavity.

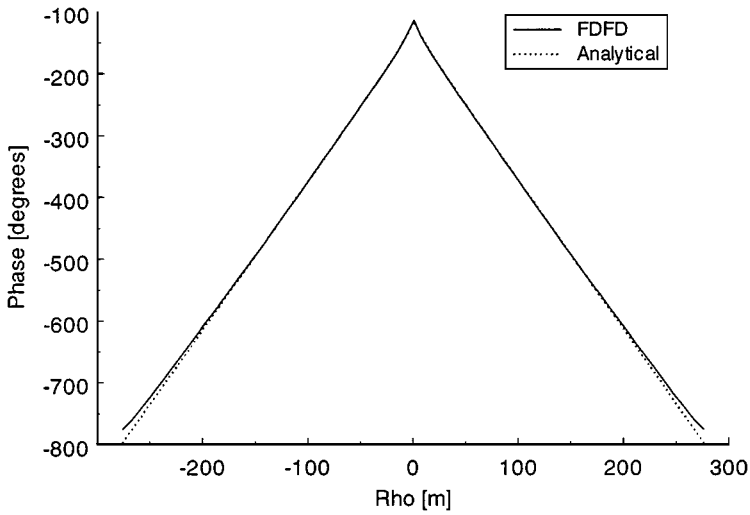

FIG. 8. The phase of E_z for the square cavity.

choice of tolerance (10^{-5}). The smallest tolerance (10^{-7}) required about 3.4 h and 1200 iterations. This computation was serial and required about 700 MB of memory. In Figs. 10 and 11 the results of the code calculations for the magnetic field magnitude and phase are compared with those for the same model obtained using the code EM1D (based on a semianalytical formula for such layered models) developed by Ki-Ha Lee at LBNL. The observed agreement is good for all choices of convergence tolerance, but becomes excellent for the two smallest values.

Since the buried resistive layer might be viewed as an easy case for the PML because the majority of the medium is conducting and therefore helping to attenuate the signal—

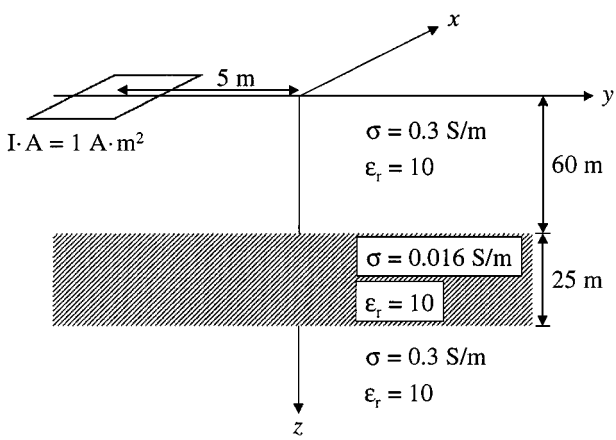

FIG. 9. Current loop at the surface of the medium with a buried resistive layer. The same basic picture also applies to our second example with a buried conducting layer, but the conductivity values are reversed (0.3 ↔ 0.016) in this case.

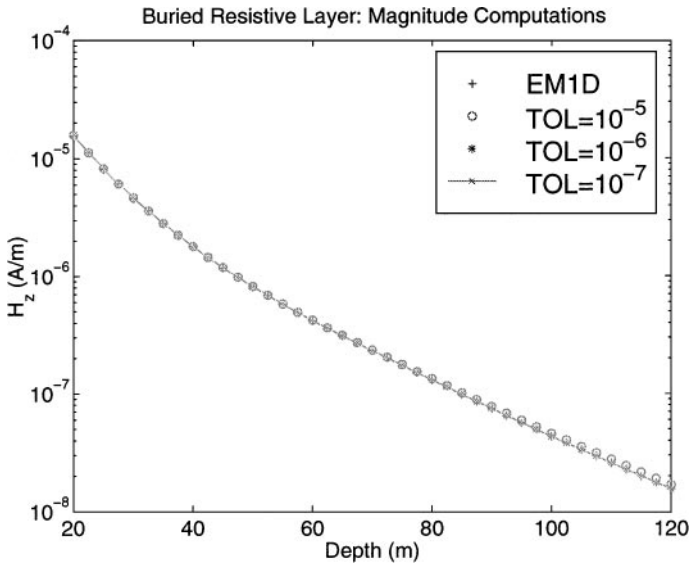

FIG. 10. Comparison of FDFD computed magnitude of magnetic field in the layered model with buried resistive layer in Fig. 9 with semianalytic results from EM1D of Ki-Ha Lee (LBNL). The two smaller choices of convergence tolerance give virtually the same results for this example, and are in good agreement with EM1D.

perhaps obviating the need for the PML—we have also tested the code for the reverse problem of a buried conductive layer in a resistive background. All other parameters are the same, including those used for the PML. The computation was performed as in the previous example and required approximately 3.3 h of CPU time using about 1150 iterations to achieve convergence (with observed excellent agreement) for the intermediate choice of

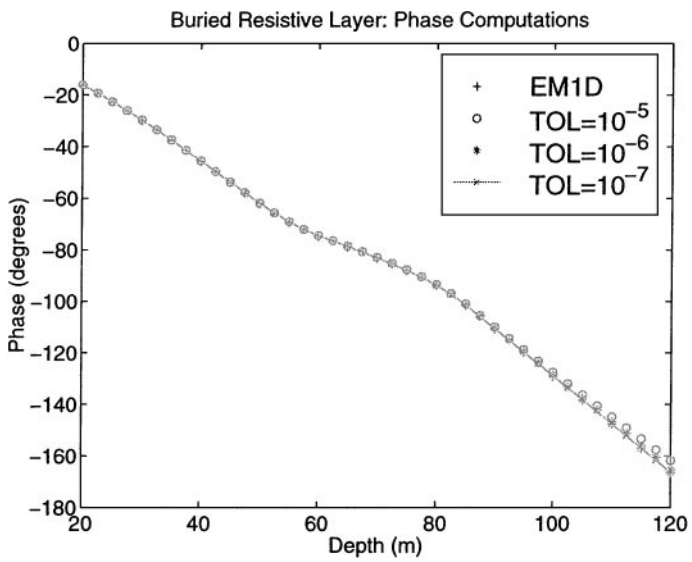

FIG. 11. Comparison of FDFD computed phase of magnetic field in the layered model with buried resistive layer in Fig. 9 with semianalytic results from EM1D of Ki-Ha Lee (LBNL). The smallest choice of convergence tolerance gives virtually the same results as EM1D for this example, while the other two are also in good agreement.

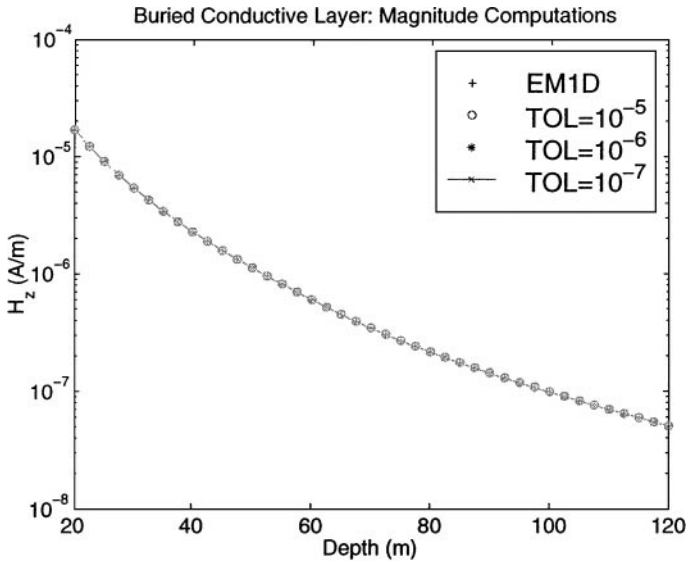

FIG. 12. Comparison of FDFD computed magnitude of magnetic field in the layered model with buried conductive layer as in Fig. 9 (but reversing the values $0.3 \leftrightarrow 0.016$) with those from EM1D. All three choices of convergence tolerance give virtually the same results for this example, and are in good agreement with EM1D.

tolerance (10^{-6}). The smallest tolerance (10^{-7}) required about 7.5 h and 2700 iterations. In Figs. 12 and 13 the results of the code calculations for the magnetic field magnitude and phase are again compared with those for the same model obtained using the code EM1D developed by Ki-Ha Lee at LBNL. The observed agreement is excellent for the two smallest choices of convergence tolerance, but the resistive background case clearly

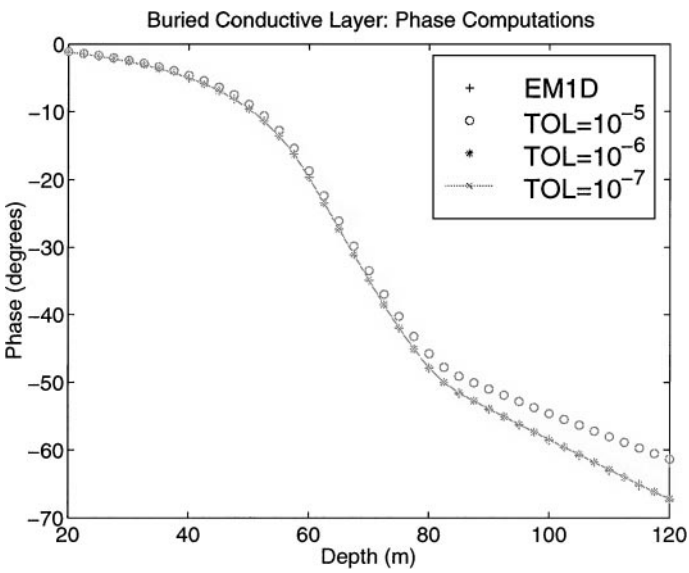

FIG. 13. Comparison of FDFD computed phase of magnetic field in the layered model with buried resistive layer in Fig. 9 (but reversing the values $0.3 \leftrightarrow 0.016$) with those from EM1D. The largest deviation from EM1D is observed here for the largest choice of convergence tolerance, while the two smallest values give virtually the same results as EM1D for this example.

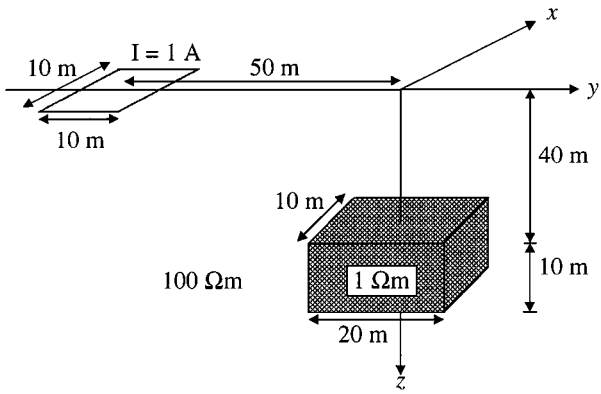

FIG. 14. Current loop at the surface of the medium with a conductive body buried in a homogeneous half-space as in [26]. The frequency of operation is 1 kHz.

is harder to compute since the worst agreement seen here is for the phase at large depths, when the largest choice of convergence tolerance (10^{-5}) was in use.

Finally, consider the geometry shown in Fig. 14. which depicts a conductive body buried within a homogeneous half-space with a rectangular loop of current as the excitation. The frequency of operation is 1 kHz. The x component of the electric field and the z component of the magnetic field are sampled along the y axis about the origin. The magnitude and phase of the electric field are shown in Figs. 15 and 16. The magnitude and phase of the magnetic field are displayed in Figs. 17 and 18. In each plot data from codes described in [26] are compared against data generated by FDFD. The three curves used in the comparisons to FDFD are (a) IE for the full integral equation solution, (b) QRS for the quasi-linear approximation using the simplest scalar reflectivity tensor, and (c) QRD for the quasi-linear approximation using the diagonal reflectivity tensor. FDFD produces results similar to those obtained from IE, QRS, and QRD for both the electric and magnetic fields in all cases. FDFD

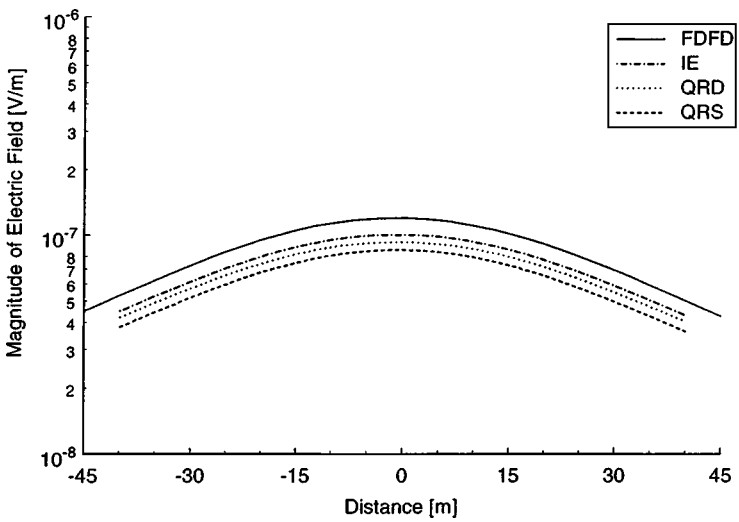

FIG. 15. Comparison of the scattered electric field magnitude for the model in Fig. 13. The fields are sampled along the y axis about the origin.

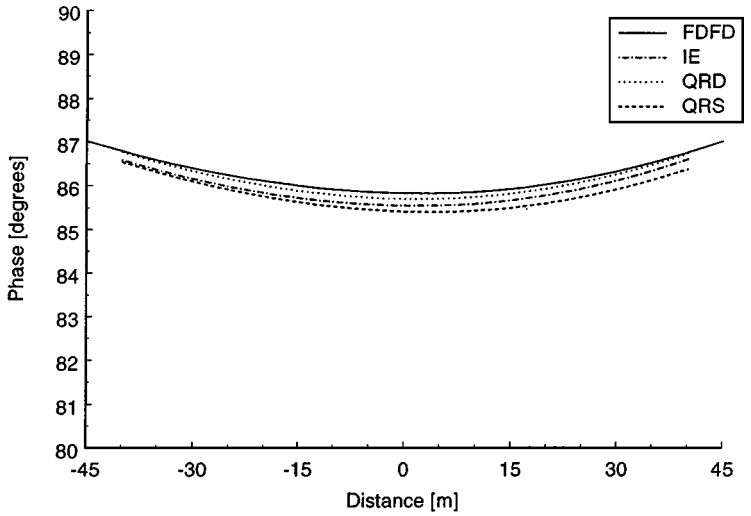

FIG. 16. Comparison of the scattered electric field phase for the model in Fig. 13. The fields are sampled along the *y* axis about the origin.

is seen to be especially good at finding the dip in the magnetic field magnitude in Fig. 17 and at approximating the magnetic field phase in Fig. 18.

5. EM DATA INVERSION USING THE ADJOINT FIELD METHOD

The EM forward modeling capability was developed here with the ultimate goal of providing the tools needed for a fully nonlinear inversion technique for electromagnetic induction tomography. Working in parallel, Dorn *et al*. [21] have developed a new approach to the inverse problem of electromagnetics based on the so-called "adjoint field technique."

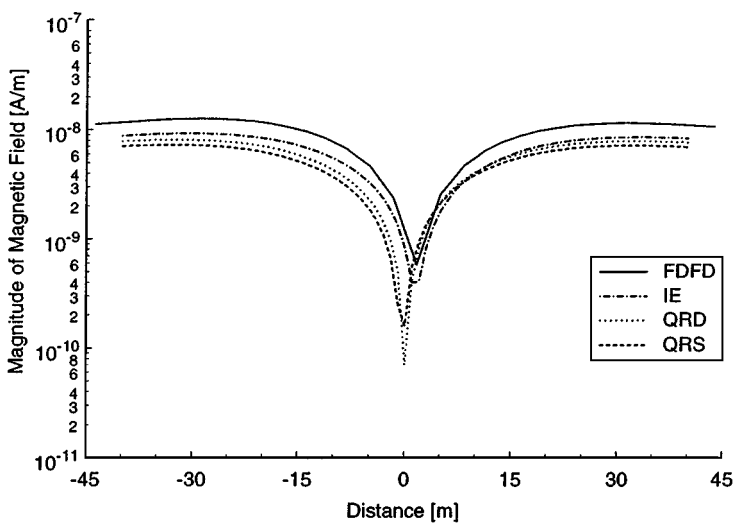

FIG. 17. Comparison of the scattered magnetic field magnitude for the model in Fig. 13. The fields are sampled along the *y* axis about the origin.

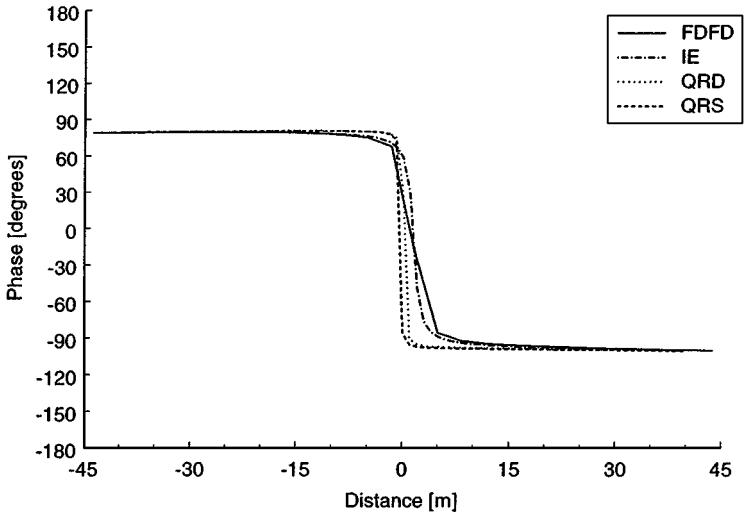

FIG. 18. Comparison of the scattered magnetic field phase for the model in Fig. 13. The fields are sampled along the *y* axis about the origin.

This method has the very useful property that the inverse problem can be solved in an iterative fashion by making two uses of the same forward modeling code we have developed and validated here. Using a somewhat oversimplified description of this technique, the updates to the electrical conductivity distribution are obtained by first making one pass through the forward solver using the latest best guess of the nature of the conducting medium, and then another pass with the adjoint operator (which, except for some minor differences in the boundary conditions, is just the conjugate transpose of the forward modeling operator) applied to the differences in computed and measured data. Then the results of these two calculations are combined to determine updates to the original conductivity model. The resulting procedure is iterative and can be applied successively to parts of the data, e.g., data associated with one transmitter location can be used to update the model before other transmitter locations are considered. This procedure has several of the same advantages as the very well tested method of wave-equation migration in reflection seismology [32] and is also related to more recent methods in electromagnetics introduced by Zhdanov *et al.* [33].

We refer the reader to the published account [21] of these applications of the present code to the data inversion problem for EMIT for more details.

6. CONCLUSIONS

A new code for 3D electromagnetics in the presence of highly conducting media has been developed and validated here. The method has already been shown elsewhere [21] to provide all the tools required for constructing a new nonlinear computational inversion scheme for imaging high-contrast electrical conductors in the earth, based on an adjoint field reconstruction method. Results obtained from this inversion method for such high-contrast media are encouraging and provide a significant improvement over results obtained from linearized inversion methods such as the Born approximation [3].

APPENDIX

Various special symbols used in this paper will now be defined. First, x_m, y_m, and z_m are the edge lengths of the mth cell (Fig. 2) in the x, y, and z directions, respectively. Additional lengths associated with the magnetic fields (staggered grid cell lengths) are given by

$$\bar{x}_m = \frac{x_m + x_d}{2}, \qquad \bar{y}_m = \frac{y_m + y_l}{2}, \qquad \bar{z}_m = \frac{z_m + z_f}{2}. \tag{A.1}$$

Then, the area of the staggered grid cell face is given by

$$\begin{aligned} a_{m_x} &= \frac{y_m z_m + y_l z_l + y_f z_f + y_{lf} z_{lf}}{4}, \\ a_{m_y} &= \frac{x_m z_m + x_d z_d + x_f z_f + x_{df} z_{df}}{4}, \\ a_{m_z} &= \frac{x_m y_m + x_d y_d + x_l y_l + x_{dl} y_{dl}}{4} \end{aligned} \tag{A.2}$$

in the x, y, and z directions, respectively. Next, the permittivities associated with the electric field at an edge are given by

$$\begin{aligned} \bar{\varepsilon}_{m_{xx}} &= \frac{y_m z_m \varepsilon_{m_{xx}} + y_l z_l \varepsilon_{l_{xx}} + y_f z_f \varepsilon_{f_{xx}} + y_{lf} z_{lf} \varepsilon_{lf_{xx}}}{4}, \\ \bar{\varepsilon}_{m_{yy}} &= \frac{x_m z_m \varepsilon_{m_{yy}} + x_d z_d \varepsilon_{d_{yy}} + x_f z_f \varepsilon_{f_{yy}} + x_{df} z_{df} \varepsilon_{df_{yy}}}{4}, \\ \bar{\varepsilon}_{m_{zz}} &= \frac{x_m y_m \varepsilon_{m_{zz}} + x_d y_d \varepsilon_{d_{zz}} + x_l y_l \varepsilon_{l_{zz}} + x_{dl} y_{dl} \varepsilon_{dl_{zz}}}{4}. \end{aligned} \tag{A.3}$$

Finally, the magnetic permeabilities associated with the magnetic field component at a face are given by

$$\begin{aligned} \bar{\mu}_{m_{xx}} &= \frac{\mu_{m_{xx}} \mu_{d_{xx}} (x_m + x_d)}{\left(x_m \mu_{d_{xx}} + x_d \mu_{m_{xx}}\right)}, \\ \bar{\mu}_{m_{yy}} &= \frac{\mu_{m_{yy}} \mu_{l_{yy}} (y_m + y_l)}{\left(y_m \mu_{l_{yy}} + y_l \mu_{m_{yy}}\right)}, \\ \bar{\mu}_{m_{zz}} &= \frac{\mu_{m_{zz}} \mu_{f_{zz}} (z_m + z_f)}{\left(z_m \mu_{f_{zz}} + z_f \mu_{m_{zz}}\right)}. \end{aligned} \tag{A.4}$$

The set of all these cell quantities is represented using matrices as

$$\begin{aligned} \boldsymbol{D}_\ell &= \mathrm{Diag}(\ldots, z_m, y_m, z_m, \ldots), \\ \boldsymbol{D}_{\bar{\ell}} &= \mathrm{Diag}(\ldots, \bar{z}_m, \bar{y}_m, \bar{x}_m, \ldots), \end{aligned} \tag{A.5}$$

$$\begin{aligned} \boldsymbol{D}_A &= \mathrm{Diag}(\ldots, x_m y_m, x_m z_m, y_m z_m, \ldots), \\ \boldsymbol{D}_{\bar{A}} &= \mathrm{Diag}\big(\ldots, a_{m_z}, a_{m_y}, a_{m_x}, \ldots\big), \end{aligned} \tag{A.6}$$

$$\begin{aligned} \boldsymbol{D}_{A\varepsilon} &= \mathrm{Diag}\big(\ldots, \bar{\varepsilon}_{m_{zz}}, \bar{\varepsilon}_{m_{yy}}, \bar{\varepsilon}_{m_{xx}}, \ldots\big), \\ \boldsymbol{D}_{\mu} &= \mathrm{Diag}\big(\ldots, \bar{\mu}_{m_{zz}}, \bar{\mu}_{m_{yy}}, \bar{\mu}_{m_{xx}}, \ldots\big). \end{aligned} \tag{A.7}$$

Additionally, the volume matrix is given by

$$\boldsymbol{D}_{V\varepsilon\varepsilon} = \mathrm{Diag}\big(\ldots, V_{m_z}, V_{m_y}, V_{m_x}, \ldots\big), \tag{A.8}$$

where

$$V_{m_\alpha} = \frac{1}{8}\Big[\left|\varepsilon_{m_{\alpha\alpha}}\right|^2 x_m y_m z_m + \left|\varepsilon_{d_{\alpha\alpha}}\right|^2 x_d y_d z_d + \left|\varepsilon_{l_{\alpha\alpha}}\right|^2 x_l y_l z_l + \left|\varepsilon_{f_{\alpha\alpha}}\right|^2 x_f y_f z_f + \left|\varepsilon_{df_{\alpha\alpha}}\right|^2 x_{df} y_{df} z_{df} + \left|\varepsilon_{dl_{\alpha\alpha}}\right|^2 x_{dl} y_{dl} z_{dl} + \left|\varepsilon_{lf_{\alpha\alpha}}\right|^2 x_{lf} y_{lf} z_{lf} + \left|\varepsilon_{dlf_{\alpha\alpha}}\right|^2 x_{dlf} y_{dlf} z_{dlf}\Big]. \tag{A.9}$$

The vectors $\vec{e}$, $\vec{h}$, $\vec{j}$, and $\vec{m}$ have the general form

$$\vec{f} = \left(\ldots, F_{m_z}, F_{m_y}, F_{m_x}, \ldots\right). \tag{A.10}$$

Finally, the coefficient matrices $\boldsymbol{A}$ and $\boldsymbol{B}$ are given as in Beilenhoff *et al.* [19] and, therefore, will not be repeated here.

ACKNOWLEDGMENTS

We thank J. B. Grant and R. M. Sharpe for helping to establish the directions we would take in the EM forward modeling code development for this problem. Also, our thanks to M. S. Zhdanov and E. Tartaras for providing us with some numerical data from the codes described in [26].

REFERENCES

1. W. M. Telford, L. P. Geldart, R. E. Sheriff, and D. A. Keys, *Applied Geophysics* (Cambridge Univ. Press, Cambridge, UK, 1976), Section 3.5.4.
2. A. Ramirez, W. D. Daily, D. LaBrecque, E. Owen, and D. Chesnut, Monitoring an underground steam injection process using electrical resistance tomography, *Water Resour. Res.* **29**, 73 (1993).
3. D. L. Alumbaugh, *Iterative Electromagnetic Born Inversion Applied to Earth Conductivity Imaging*, Ph.D. thesis (University of California, Berkeley, 1993).
4. H.-W. Tseng, A. Becker, M. J. Wilt, and M. Deszcz-Pan, A borehole-to-surface electromagnetic survey, *Geophys.* **73**, 1565 (1998).
5. F. Ebeling, R. Klatt, F. Krawczyk, E. Lawinsky, T. Weiland, S. G. Wipf, B. Steffen, T. Barts, M. J. Browman, R. K. Cooper, H. Deaven, and G. Rodenz, The 3-D MAFIA group of electromagnetic codes, *IEEE Trans. Magn.* **25**, 2962 (1989).
6. M. Dehler, M. Dohlus, A. Fischerauer, G. Fischerauer, P. Hahne, P. Klatt, F. Krawczyk, T. Propper, P. Schutt, T. Weiland, F. Ebeling, M. Marx, S. G. Wipf, B. Steffen, T. Barts, J. Browman, R. K. Cooper, G. Rodenz, and D. Rusthoi, Status and future of the 3D-MAFIA group of codes, *IEEE Trans. Magn.* **26**, 751 (1990).
7. J. P. Berenger, A perfectly matched layer for the absorption of electromagnetic waves, *J. Comput. Phys.* **114**, 185 (1994).
8. G. W. Hohmann, Numerical modeling for electromagnetic methods of geophysics, in *Electromagnetic Methods in Applied Geophysics Volume 1, Theory*, edited by M. N. Nabighian, Society of Exploration Geophysicists (Tulsa, Oklahoma, 1987), pp. 314–363.
9. R. L. Mackie, J. T. Smith, and T. R. Madden, 3-Dimensional electromagnetic modeling using finite-difference equations—The magnetotelluric example, *Radio Sci.* **29**, 923 (1994).
10. C. Torres-Verdin and T. M. Habashy, Rapid 2.5-dimensional forward modeling and inversion via a new nonlinear scattering approximation, *Radio Sci.* **29**, 1051 (1994).
11. G. A. Newman and D. L. Alumbaugh, Frequency-domain modeling of airborne electromagnetic responses using staggered finite-differences, *Geophys. Prospecting* **43**, 1021 (1995).
12. G. A. Newman and D. L. Alumbaugh, Three-dimensional massively parallel electromagnetic inversion. 1. Theory, *Geophys. J. Int.* **128**, 345 (1997).

13. G. A. Newman and D. L. Alumbaugh, Three-dimensional magnetotelluric inversion using nonlinear conjugate gradients, *Geophys. J. Int.* **140**, 410 (2000).
14. J. T. Smith, Conservative modeling of 3-D electromagnetic fields. Part I. Properties and error analysis, *Geophys.* **61**, 1308 (1996).
15. J. T. Smith, Conservative modeling of 3-D electromagnetic fields. Part II. Biconjugate graident solution and an accelerator, *Geophys.* **61**, 1319 (1996).
16. M. S. Zhdanov, I. M. Varentsov, J. T. Weaver, N. G. Golubev, and V. A. Krylov, Methods for modeling electromagnetic fields: Results from COMMEMI—The international project on the comparison of modeling methods for electromagnetic induction, *J. Appl. Geophys.* **37**, 133 (1997).
17. M. J. Wilt, D. L. Alumbaugh, H. F. Morrison, A. Becker, K. H. Lee, and M. Deszcz-Pan, Cross-well electromagnetic tomography: System design considerations and field results, *Geophys.* **60**, 871 (1995).
18. H. M. Buettner and J. G. Berryman, An electromagnetic induction tomography field experiment at Lost Hills, CA, in *Proceedings of the Symposium on the Application of Geophysics to Engineering and Environmental Problems (SAGEEP), Oakland, CA*, March 14–18, 1999, pp. 663–672.
19. K. Beilenhoff, W. Heinrich, and H. L. Hartnagel, Improved finite-difference formulation in frequency domain for three-dimensional scattering problems, *IEEE Trans. Microwave Theor. Tech.* **40**, 540 (1992).
20. J. Y. Wu, D. M. Kingsland, J. F. Lee, and R. Lee, A comparison of anisotropic PML to Berenger's PML and its application to the finite-element method for EM scattering, *IEEE Trans. Antennas Prop.* **45**, 40 (1997).
21. O. Dorn, H. Bertete-Aguirre, J. G. Berryman, and G. C. Papanicolaou, A nonlinear inversion method for 3D-electromagnetic imaging using adjoint fields, *Inverse Probl.* **15**, 1523 (1999).
22. J. L. Davis and A. P. Annan, Ground penetrating radar for high resolution mapping of soil and rock stratigraphy, *Geophys. Prospect.* **37**, 531 (1989).
23. E. Fisher, G. A. McMechan, and A. P. Annan, Acquisition and processing of wide-aperature ground penetrating radar data, *Geophys.* **57**, 495 (1992).
24. Z. S. Sacks, D. M. Kingsland, R. Lee, and J. F. Lee, A perfectly matched anisotropic absorber for use as an absorbing boundary condition, *IEEE Trans. Antennas Prop.* **43**, 1460 (1995).
25. M. Kuzuoglu and R. Mittra, Frequency dependence of the constitutive parameters of causal perfectly matched anisotropic absorbers, *IEEE Microwave Guided Wave Lett.* **6**, 447 (1996).
26. M. S. Zhdanov and S. Feng, Quasi-linear approximation in 3D electromagnetic modeling, *Geophys.* **61**, 646 (1996).
27. T. T. Wu and R. W. P. King, The cylindrical antenna with nonreflecting resisitive loading, *IEEE Trans. Antennas Prop.* **13**, 369 (1965).
28. N. J. Champagne, J. T. Williams, R. M. Sharpe, S. U. Hwu, and D. R. Wilton, Numerical modeling of impedance loaded multi-arm archimedian spiral antennas, *IEEE Trans. Antennas Prop.* **40**, 102 (1992).
29. H. A. van der Vorst, Bi-CGSTAB: A fast and smoothly converging variant of Bi-CG for the solution of non-symmetric linear systems, *SIAM J. Sci. Stat. Comput.* **13**, 631 (1992).
30. H. A. van der Vorst, Minimum residual modifications to Bi-CG and to the preconditioner, in *Recent Advances in Iterative Methods*, edited by G. Golub, A. Greenbaum, and M. Luskin (Springer-Verlag, New York, 1994), pp. 217–225.
31. V. L. Druskin, L. A. Knizhnerman, and P. Lee, New spectral Lanczos decomposition method for induction modeling in arbitrary 3-D geometry, *Geophys.* **64**, 701 (1999).
32. J. F. Claerbout, *Fundamentals of Geophysical Data Processing: With Applications to Petroleum Prospecting* (McGraw-Hill, New York, 1976).
33. M. S. Zhdanov, P. Traynin, and J. R. Booker, Underground imaging by frequency-domain electromagnetic migration, *Geophys.* **61**, 666 (1996).